Subnanometer-scale size effects in electronic spectra of Si/SiO_2 multiple quantum wells: Interferometric second-harmonic generation spectroscopy

V. G. Avramenko, T. V. Dolgova, A. A. Nikulin, A. A. Fedyanin, and O. A. Aktsipetrov
Department of Physics, M.V. Lomonosov Moscow State University, Moscow 119992, Russia

A. F. Pudonin
P.N. Lebedev Physical Institute, Russian Academy of Science, 177924 Moscow, Russia

A. G. Sutyrin, D. Yu. Prokhorov, and A. A. Lomov
A.V. Shubnikov Institute of Crystallography, Russian Academy of Science, 119333 Moscow, Russia
(Received 25 October 2005; revised manuscript received 17 February 2006; published 19 April 2006)

Resonant electronic structure of amorphous-Si/SiO_2 multiple quantum wells (MQWs) is studied by means of second-harmonic generation (SHG) spectroscopy and SHG interferometric spectroscopy of the MQW samples with the Si quantum well thickness d ranging from 1.00 to 0.25 nm. The observed modification of the SHG spectra upon decreasing d is interpreted using a combination of the resonant two-subband approximation for the nonlocal optical response of each quantum well with the generalized transfer-matrix formalism for the description of light propagation across the whole MQW structure. Agreement with the experiment shows that the description of the quadratic optical response of the MQW structure within the model of a nonlocal piecewise-continuous medium remains valid on the subnanometer scale.

DOI: 10.1103/PhysRevB.73.155321 PACS number(s): 78.67.De, 73.21.Fg, 42.65.−k

I. INTRODUCTION

Typically, amorphous-Si/SiO_2 superlattices are referred to as Si/SiO_2 multiple quantum wells (MQWs) because of a large mismatch [about 7 eV (Ref. 1)] in the band gap widths of bulk Si and SiO_2, which makes the electron tunneling between adjacent quantum wells negligible. In the past decade various optical phenomena in these heterostructures have been intensively studied: linear reflection,[2] luminescence,[3,4] x-ray absorption,[5] second-harmonic generation (SHG),[6–8] and dc-electric-field-induced SHG.[9–11] Due to size quantization of the electron motion across the quantum wells, spectral properties of MQWs are very sensitive to the value of the average Si quantum well thickness d. The preparation procedure allows obtaining MQW samples with d ranging down to subnanometer values. This imposes the question: which of the models of the optical response remain applicable to SHG description in MQWs with subnanometer values of d? The microscopic description of the quadratic response of amorphous-silicon quantum wells is usually based on the models of the electronic properties that ignore the morphological details of thin amorphous-silicon layers [in contrast, e.g., to the Si(001)-adsorbate system for which detailed *ab initio* calculations of the quadratic optical susceptibility have been carried out[12]]. In the direction normal to the quantum-well plane the layered structure is modeled by piecewise-constant spatial modulation of the physical parameters characterizing the system (e.g., the band gap width), with the interfaces being assumed to be ideally planar. Although such models become inadequate to the real (discrete) morphology of subnanometer-thick quantum wells, one can expect that for the description of the macroscopic optical properties of the MQW system these models remain applicable even on the subnanometer scale. In Ref. 3 it was shown that the photoluminescence peak shift observed upon varying d within the range of 1–3 nm is proportional to d^{-2}, which is consistent with the simplest model based on the the effective-mass approximation with infinite potential barriers. By contrast, within the subnanometer range $d \sim 0.25-1$ nm the peak shift observed in second-harmonic spectra was found to significantly deviate from the d^{-2} dependence (the latter is much steeper). In order to explain this discrepancy, some of the factors affecting the potential well shape, namely, the image-potential correction,[13] finite depth,[8] and interfacial distortion,[8] were taken into account within the effective mass approximation. It was shown[8] that only the third of them is capable of "flattening" the dependence on d to the degree comparable with the experiment. However, in the context of second-harmonic spectroscopy of MQWs the role of far-ranging electromagnetic interaction between quantum wells was treated in an oversimplified manner.[8] Meanwhile, it is far-ranging electromagnetic interaction between quantum wells in the MQW structure that modifies the spectral properties of the system as compared to those of a single Si quantum well in a SiO_2 host and can be, in principle, another source of size effects in the quadratic optical response of MQWs. Described within the current-sheet formalism,[14,15] this interaction was shown to affect essentially the linear-reflection spectra of Si/SiO_2 MQWs.[2]

Even though the electron spectrum of Si/SiO_2 MWQs was studied previously using different techniques of linear optics,[2,16,17] SHG spectroscopy has several advantages. In centrosymmetric media the quadratic polarization vanishes in the electric-dipole approximation and is determined by the next-order (quadrupole) term of the multipole expansion.[18] Due to large number of interfaces in MQWs, second-harmonic generation, which is an intrinsically interface-sensitive technique, is expected to be a particularly suitable

probe for these structures.[18] Quadratic susceptibility of Si/SiO_2 MQWs is also expected to be enhanced due to the large electric field discontinuity resulting from the significant difference in dielectric constants of wells and barriers. Therefore, in MQWs fabricated on top of a centrosymmetric substrate, the MQW-to-substrate signals ratio becomes significantly better for SHG than for conventional linear optical techniques, such as reflection[2,16] and absorption[17] spectroscopy. Additionally, probing virtual electron resonances at both fundamental and second-harmonic (SH) photon energies simultaneously, SHG spectroscopy allows studying the electron spectrum in the energy region up to 5 eV, which is difficult for linear optics techniques. For example, this paper reports observation of new resonance features in the spectral region from 3.7 to 4.0 eV, which was not studied in previous linear-optical measurements.

In this paper, the second-harmonic spectra of Si/SiO_2 MQWs with the Si quantum well thickness varying within the subnanometer range (0.25–1 nm) are studied both experimentally and theoretically. The experimental part of the work (Sec. II) is based on combining the SH intensity measurements with the SHG interferometry. This allows one to characterize the second-harmonic signal from the studied samples with two real parameters, namely, with the modulus A and the argument ϕ of the complex SH wave amplitude $Ae^{i\phi}$ (instead of the conventional one-parameter characterization provided by the intensity measurements proper). We call A and ϕ the SH wave amplitude and phase, respectively. The intensity measurements yield the amplitude A, whereas handling the SHG interference patterns yields the difference of the phases $\phi-\phi_{\mathrm{ref}}$, where ϕ_{ref} is the SH wave phase of the signal from the reference SH source. Besides, the rotational (azimuthal) dependence of the SH intensity is measured, which allows determining another relative phase, namely, the phase shift between the isotropic and anisotropic components of the SH signal. We call this quantity the anisotropy phase $\tilde{\varphi}$. The thickness dependence of the spectrum of $\tilde{\varphi}$ can characterize the nonuniformity of the in-plane symmetry of Si quantum wells in the normal direction, from the substrate towards the outer interface. The theoretical part of the work is presented in Sec. III and the Appendix. To describe the propagation of the fundamental and SH waves across the MQW structure we consider a nonlocal generalization of the optical transfer-matrix technique introduced in Ref. 19. In Sec. IV both phenomenological analysis and numerical calculations based on the results of Sec. III are applied to interpretation of the experimental data.

II. EXPERIMENTAL

A. Experimental setups

SHG spectroscopy is performed using a tunable nanosecond parametric generator/amplifier laser system as a source of p-polarized fundamental radiation. The operating intervals in the idler and signal wavelength ranges are 745–1000 nm and 490–680 nm, respectively, with the pulse duration of 4 ns and energy of about 10 mJ per pulse. The reflected p-polarized SH wave is spectrally separated by a set of filters and detected by a photomultiplier tube and an electronic peak-hold detector. The reference channel is used for normalizing the SH intensity spectrum over the laser fluence and the spectral sensitivity of the optical detection system. A slightly wedged z-cut quartz plate is used as a source of the reference SH signal and the detection system is identical to the system in the sample channel.

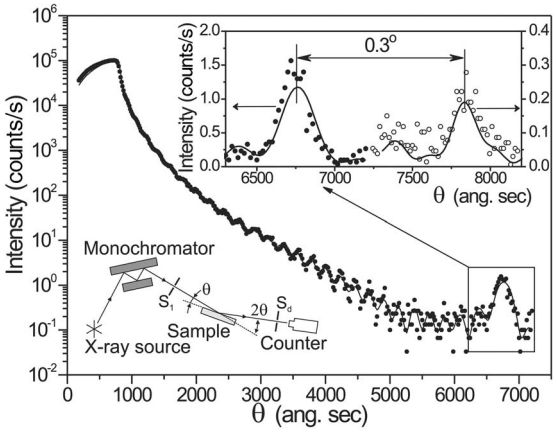

FIG. 1. Angular dependence of x-ray reflection from sample 1: experimental data (filled circles) and results of the fitting (solid curve). Upper inset enlarges in the linear scale the first Bragg peak for sample 1 (filled circles) and shows its angular shift with respect to that for sample 2 (open circles). Lower inset: schematic of experimental setup for x-ray reflectometry utilizing triple-axis diffractometer.

The SH wave-phase spectra are measured with the use of the second-harmonic interferometric spectroscopy technique based on the single-wavelength second-harmonic interferometry and described in detail in Ref. 20. A spectrum of the relative SH wave phase is extracted from a set of SHG interferograms measured at different wavelengths. Each SHG interferogram is obtained by translating the reference along the laser beam in order to change the distance between the sample and the reference. The latter is a 30 nm thick indium tin oxide (ITO) film on a 1 mm thick plate of fused quartz. The phase spectra are normalized to the ITO phase spectra measured in the reflection geometry, replacing the sample with a thick quartz plate with the immersed rear interface.

The morphology of the samples is studied by high-resolution x-ray reflectometry using a triple-axis diffractometer technique. The schematic of experimental setup is shown in the inset in Fig. 1. A conventional 1.0 kW x-ray tube with a copper anode is used as a radiation source. The highly-collimated x-ray beam is obtained using a grooved triple Ge(004) monochromator and collimating slits (S_1) and has 20 μm in width and 2 mm in height. The actual divergency of the x-ray beam in the scattering plane is limited to about 30 arc s. The reflected intensity is measured with the step of 10 arc s in the longitudinal $\theta/2\theta$ scan, with θ and 2θ being the incidence angle and the angular position of the scintillation counter with respect to the incident beam, respectively. A vertical slit (S_d) with an angular aperture of 2 arc min is placed in front of the counter and used for reduction of the background contribution and most of the diffuse scattering. The background intensity is measured in the longitudinal scan at the fixed $\pm 2'$ offset from the sample

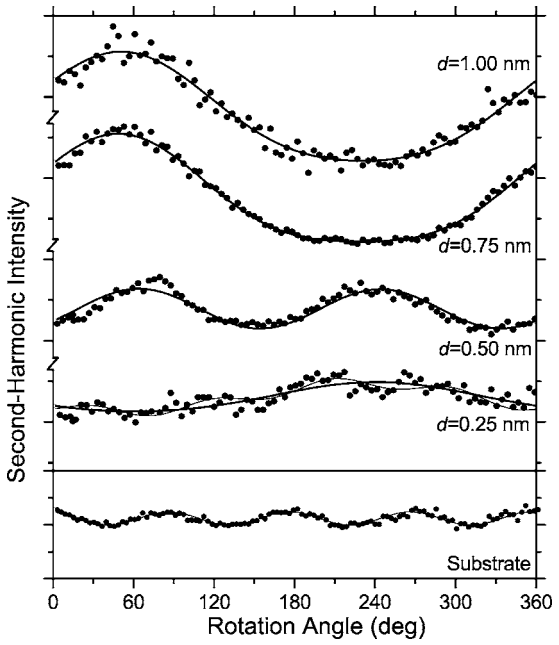

FIG. 2. Top panel: SH intensity measured for different MQW samples as a function of the azimuthal angle at the p-in, p-out polarizations combination and $2\hbar\omega=4.35$ eV. Solid curves: numerical results of fitting Eq. (1) to the experimental data. For sample 4 ($d=0.25$ nm) the fitting results obtained by including the fourth azimuthal Fourier harmonic in Eq. (1) are also shown (thinner curve). Bottom panel: rotational dependence of the p-in, p-out SHG signal from the bare Si(001) substrate measured at $2\hbar\omega=3.9$ eV.

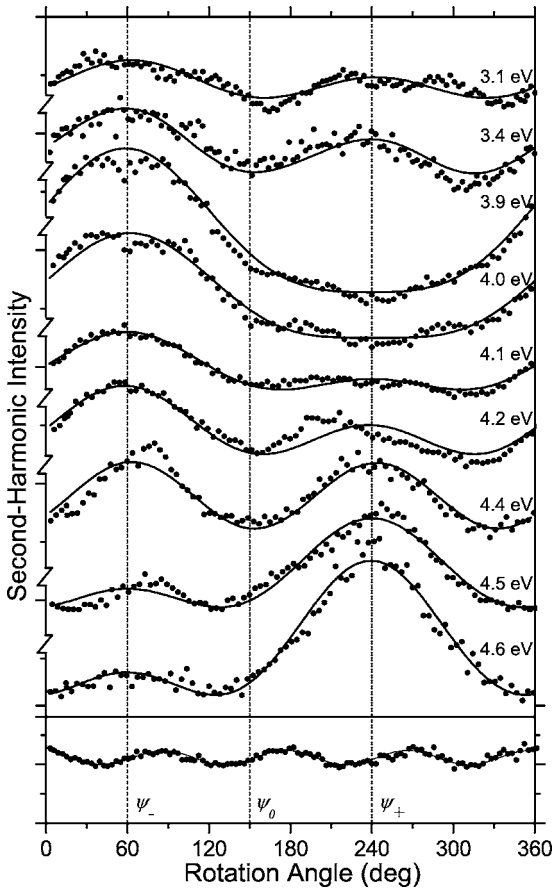

FIG. 3. Top panel: SH intensity measured for sample 3 as a function of the azimuthal angle at the p-in, p-out polarizations combination and various values of the SH photon energy. Solid curves: numerical results of fitting of Eq. (1) to the experimental data. Vertical lines denote the characteristic angles ψ_0 and $\psi_\pm=\psi_0\pm90°$. Bottom panel: same as in the bottom panel of Fig. 2 (shown as a reference: noteworthily, the angle ψ_0 is the same for both the MQW sample and bare substrate).

arrangement position and then is subtracted from the specular intensity data.

B. Samples and their diagnostics

The studied MQW samples are layered structures with alternating layers of amorphous silicon and silicon dioxide grown by rf sputtering of silicon and fused quartz targets in an argon plasma discharge in a vacuum chamber with the residual pressure of 7.5×10^{-4} Torr. The preparation procedure is described in detail in Ref. 1. Four samples with silicon layer thickness d of 1.00, 0.75, 0.50, and 0.25 nm were fabricated. They are enumerated hereafter as samples 1, 2, 3, and 4, respectively. For each sample the SiO_2 layer thickness is fixed at 1.10 nm, whereas the number of the Si/SiO_2 bilayers (forming the "unit cells" of the MQW structure) varies with the sample from 30 to 70 in order to provide nearly the same total silicon thickness in each sample.

Figure 1 shows the angular dependence of the x-ray reflectivity measured in sample 1. Reflectivity peak at approximately 6750 arc s corresponds to the first-order Bragg reflection direction for the multilayered MQW structure and proves the presence of the periodical arrangement of silicon and silicon dioxide layers. The angular position of the Bragg peak, θ_B, is determined by the period thickness in the MQW. The number of oscillations in the reflectivity spectrum observed for $\theta<\theta_B$ correlates with the number of quantum wells. The similar angular dependence is observed for sample 2. The first-order Bragg maxima for samples 1 and 2 shown in the inset in Fig. 1 are shifted in angle by 0.3° from each other, which indicates the variation of the period thickness in the samples series.

C. SHG rotational anisotropy

Figure 2 shows the rotational (azimuthal) dependences of the SH intensity measured for the p-in, p-out polarizations combination at the fundamental wavelength of $\lambda_\omega=570$ nm, which corresponds to the two-photon energy of $2\hbar\omega=4.35$ eV. For all samples the SHG signal is found to be anisotropic upon rotation around the axis normal to the sample plane. The strongest anisotropy is observed for samples 1 ($d=1.00$ nm) and 2 ($d=0.75$ nm); the corresponding rotational dependences possess a onefold symmetry with significant isotropic background. For sample 3 ($d=0.50$ nm) the rotational dependence has a pronounced twofold component. A small fourfold component is revealed in the azimuthal SHG dependence for sample 4 ($d=0.25$ nm).

The modification of the azimuthal SHG dependences with the SH photon energy for sample 3 is shown in Fig. 3

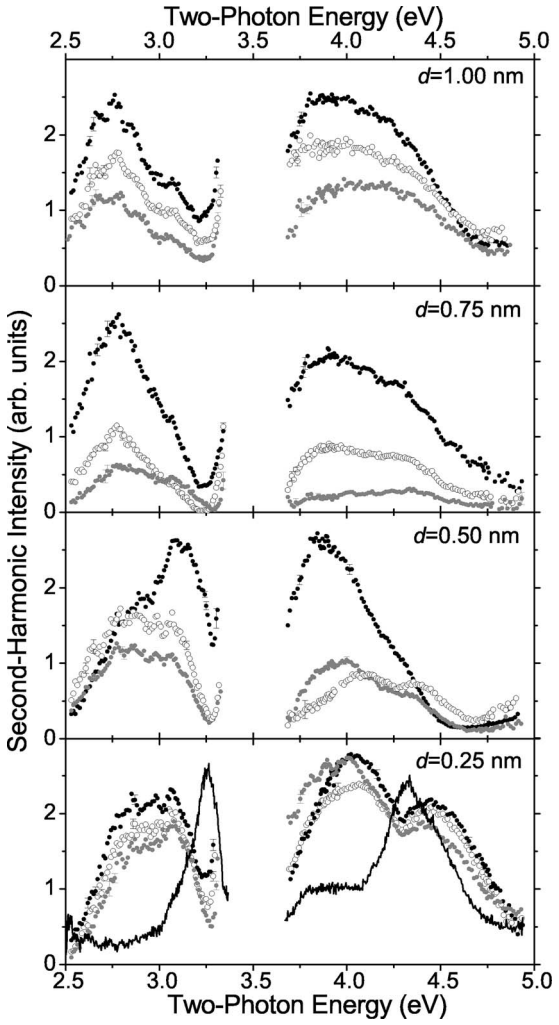

FIG. 4. SH intensity measured as a function of the two-photon energy at three azimuthal positions of the samples: ψ_0 (open circles), ψ_+ (gray circles), and ψ_- (black circles). Solid lines: SH intensity spectra of the bare Si(001) substrate.

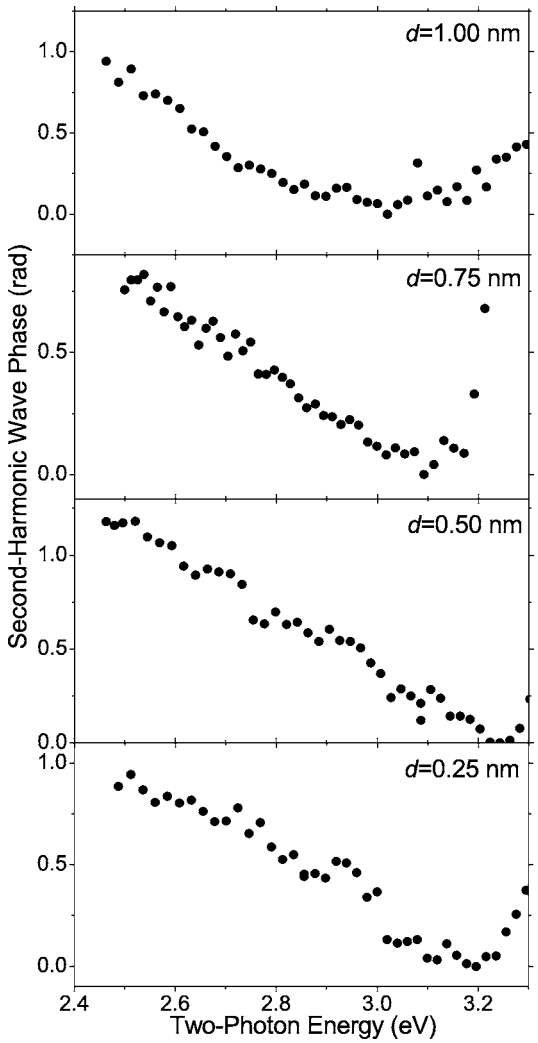

FIG. 5. Relative SH wave phase as a function of the two-photon energy at the azimuthal angle ψ_0 for which the anisotropic SH component vanishes. Every point is obtained from the fitting of the expression given by Eq. (2) to the interference pattern measured at the corresponding two-photon energy.

($d=0.5$ nm). To find the optimal azimuthal position for spectral measurements, the measured azimuthal dependences is described phenomenologically by a coherent superposition of rotationally isotropic and onefold anisotropic components of the SH field with real amplitudes E_0 and E_1, respectively, and relative phase $\tilde{\varphi}$:

$$I_{2\omega}(\psi) = |E_0 + e^{i\tilde{\varphi}} E_1 \sin(\psi - \psi_0)|^2. \quad (1)$$

At $\psi=\psi_0$ only isotropic component contributes to the SHG signal: $I_{2\omega}(\psi_0)=E_0^2$. At $\psi=\psi_+\equiv\psi_0+90°$ ($\psi=\psi_-\equiv\psi_0-90°$) constructive (destructive) interference of the isotropic and anisotropic components takes place, if $0\leqslant\tilde{\varphi}<\frac{\pi}{2}$, and, vice versa, if $\frac{\pi}{2}<\tilde{\varphi}\leqslant\pi$; the interference is absent, if $\tilde{\varphi}=\frac{\pi}{2}$. It can be seen from comparison of the top and bottom panels that the characteristic angle ψ_0 (at which the SHG signal equals the isotropic component) turns out to be the same for the MQW sample and bare Si(001) substrate, which apparently is due to the preparation procedure.

D. SHG spectroscopy

Figure 4 shows second-harmonic intensity spectra measured for three azimuthal sample positions shifted by 90° from each another and corresponding to the characteristic azimuthal angles ψ_-, ψ_0, and ψ_+. All MQW spectra exhibit resonance features in the vicinity of about 2.7 and 4 eV, in contrast to the substrate spectrum (solid line) that has a peak at 3.3 eV and a peak at 4.3 eV.

The peak shapes and positions vary for different samples. In particular, a monotonous redshift of the idler-range peak at intermediate ($\psi=\psi_0$) azimuthal position occurs as the quantum well thickness d increases.

The relative phase of the second-harmonic field is measured using SHG interferometric spectroscopy.[20] An SHG interferogram is obtained by translating a reference SHG source along the laser beam varying distance l between the reference and the sample. The result of interference of the SH waves from the reference ($E_r^{2\omega}$) and the sample ($E^{2\omega}$) is

the detected SH intensity $I=(c/8\pi)|E_r^{2\omega}+E^{2\omega}|^2$:

$$I = I_r^{2\omega} + I^{2\omega} + 2\alpha\sqrt{I_r^{2\omega}I^{2\omega}}\cos\left(\frac{2\pi l}{L(\omega)} + \Phi - \Phi_r\right), \quad (2)$$

where $L(\omega)=\lambda_\omega(2\Delta n)^{-1}$ is the interferogram period with $\Delta n=n_{2\omega}-n_\omega$ describing the air dispersion, $\Phi\equiv\mathrm{Arg}(E^{2\omega})$, $\Phi_r\equiv\mathrm{Arg}(E_r^{2\omega})+\mathrm{Arg}(R_{2\omega})$, and $\alpha\leqslant 1$ indicates the laser coherence. The deviation of α from unity appears to be very small and is neglected. $R_{2\omega}$ is the Fresnel factor of the SH wave reflection from the sample. A fit of Eq. (2) to a measured interferogram at a particular ω gives parameter Φ as the corresponding point of SH phase spectrum. Figure 5 shows a set of SH phase spectra in the idler range. Strong phase rotation—up to $\pi/2$—for all four samples confirms the resonant character of the SH spectra. The inflections that are most obvious for the 0.5 nm thick well sample may indicate the coherent superposition of two or more resonances.

III. THEORY

A. Basic macroscopic parameters

In the context of calculating the linear and quadratic optical response of an MQW structure, we consider the latter as a layered dielectric slab of thickness L. The slab consists of N Si quantum wells of thickness d each that alternate with $N+1$ SiO_2 layers of thickness D each. Obviously $L=Nl+D$, where $l=d+D$ is the spatial period of the MQW structure. The z axis is chosen to be normal to Si/SiO_2 interface planes, hence the xy plane is parallel to them. Regions $(q-1)l\leqslant z\leqslant ql-d$ with $q=1,2,\ldots,N+1$ and $ql-d\leqslant z\leqslant ql$ with $q=1,2,\ldots,N$ are occupied by dioxide layers and quantum wells, respectively. Half-spaces $z<0$ and $z>L$ correspond to vacuum and the Si substrate, respectively. The fundamental radiation, incident on the MQW structure from vacuum, is a plane p-polarized wave with frequency ω, wave vector $\mathbf{k}$, and electric field amplitude E_f. We choose the x axis to be parallel to the plane of incidence, therefore $\mathbf{k}=\{\frac{\omega}{c}\sin\theta,0,\frac{\omega}{c}\cos\theta\}$, where θ is the angle of incidence counted from the z (normal) direction. Due to translational invariance of the system in the xy plane, any quantity F determined by the optical response of the system at the fundamental and SH frequency, e.g., the induced current density, electric, or magnetic field, has the form: $F(x,z,t)=F_{n\omega}(z)\exp[in\omega(x\sin\theta/c-t)]$, where $n=1,2$. In what follows the amplitudes $F_{n\omega}(z)$ are of prime interest.

The linear optical response of the dioxide layers and the substrate is characterized by the local dielectric constants $\varepsilon(\omega)$ and $\bar{\varepsilon}(\omega)$, respectively.

Both linear and quadratic response of quantum wells are assumed to be defined by the nonlocal conductivity tensors σ and Σ, respectively; the corresponding current densities $\mathbf{j}$ and $\mathbf{J}$ induced inside the qth quantum well are as follows:

$$\mathbf{j}_{n\omega}^{(q)}(z) = \int_{ql-d}^{ql}\sigma(z-ql+d,z'-ql+d,n\omega)\cdot\mathbf{E}_{n\omega}(z')dz' \equiv \hat{\sigma}_{n\omega}^{(q)}\cdot\mathbf{E}_{n\omega}(z), \quad n=1,2, \quad (3)$$

$$\mathbf{J}^{(q)}(z) = \int_{ql-d}^{ql}\int_{ql-d}^{ql}\Sigma(z-ql+d,z'-ql+d,z''-qk+d,\omega):\mathbf{E}_\omega(z')\mathbf{E}_\omega(z'')dz'dz'' \equiv \hat{\Sigma}^{(q)}:\mathbf{E}_\omega(z)\mathbf{E}_\omega(z), \quad (4)$$

where symbols with hats are introduced for short-hand notation of corresponding integral transformations; $\mathbf{E}_n(z)$ is the local electric field at frequency $n\omega$. To avoid dealing with overcomplicated models, further theoretical considerations will be focused on the data pertaining solely to the isotropic SH component, i.e., on those measured at the intermediate azimuthal position ψ_0. This allows us to suppose for simplicity that the system is isotropic in the xy plane. Thus nonvanishing components of σ and Σ are the following: σ_{zz}, $\sigma_{xx}=\sigma_{yy}$ and Σ_{zzz}, $\Sigma_{zxx}=\Sigma_{zyy}$, $\Sigma_{xzx}=\Sigma_{yzy}$.

B. Local fields in the MQW structure

The macroscopic (electrodynamic) part of the problem consists in calculation of the local fields $\mathbf{E}_\omega(z)$ and $\mathbf{E}_{2\omega}(z)$, given the conductivity tensors. It is convenient to introduce the following notation to distinguish the values of the local field $\mathbf{E}_{n\omega}(z)$ in different regions:

$$\mathbf{E}_{n\omega}(z)\equiv\begin{cases}\mathbf{E}_{n\omega,0}(z), & z<0 \text{ (vacuum region)};\\ \mathbf{E}_{n\omega,q}(z), & (q-1)l\leqslant z\leqslant ql-d, q=1,\ldots,\\ & N+1 \text{ (qth dioxide layer)};\\ \mathbf{E}_{n\omega}^{(q)}(z), & ql-d\leqslant z\leqslant ql, q=1,\ldots,\\ & N \text{ (qth quantum well)};\\ \mathbf{E}_{n\omega,N+2}(z), & z>L \text{ (substrate)}.\end{cases}$$

For p-polarized fundamental radiation, both $\mathbf{E}_\omega(z)$ and $\mathbf{E}_{2\omega}(z)$ remain p-polarized due to the in-plane isotropy of the system. In regions with local dielectric response the field $\mathbf{E}_{n\omega}(z)$ is a superposition of rightward- and leftward-propagating p-polarized waves:

$$\mathbf{E}_{n\omega,q}(z) = E_{n\omega,q}^{+}\mathbf{e}_+e^{i\kappa_{n,q}z} + E_{n\omega,q}^{-}\mathbf{e}_-e^{-i\kappa_{n,q}z}, \quad q=0,\ldots,N+2, \quad n=1,2, \quad (5)$$

where

$$\kappa_{n\omega,0} = k_z = \frac{n\omega}{c}\cos\theta,$$

$$\kappa_{n,q=1,\ldots,N+1} = \frac{n\omega}{c}\sqrt{\varepsilon_n-\sin^2\theta}\equiv\kappa_n,$$

$$\kappa_{n,N+2} = \frac{n\omega}{c}\sqrt{\bar{\varepsilon}_n-\sin^2\theta}\equiv\bar{\kappa}_n,$$

$\varepsilon_n=\varepsilon(n\omega)$, $\bar{\varepsilon}_n=\bar{\varepsilon}(n\omega)$, and the polarization unit vectors $\mathbf{e}_+$ and $\mathbf{e}_-$ set the directions of the electric field vectors in the p-polarized rightward- and leftward-propagating waves, respectively: $\mathbf{e}_\pm=\{\pm\cos\theta,0,-\sin\theta\}$. Thus in the qth region the local field is determined by two amplitudes, $E_{n\omega,q}^{+}$ and $E_{n\omega,q}^{-}$. Obviously,

$$E^{+}_{\omega,0}(0) = E_{\mathrm{f}}, \tag{6}$$

$$E^{+}_{2\omega,0} = E^{-}_{\omega,N+2} = E^{-}_{2\omega,N+2} = 0, \tag{7}$$

$$E^{-}_{n\omega,N+1} = r_{\theta}(\varepsilon_n, \bar{\varepsilon}_n) e^{2i\kappa_n L} E^{+}_{n\omega,N+1}, \tag{8}$$

$$E^{+}_{n\omega,N+2} = t_{\theta}(\varepsilon_n, \bar{\varepsilon}_n) e^{i(\kappa_n - \bar{\kappa}_n)L} E^{+}_{n\omega,N+1},$$

$$n = 1,2, \tag{9}$$

where $r_{\theta}(\varepsilon_n, \bar{\varepsilon}_n)$ and $t_{\theta}(\varepsilon_n, \bar{\varepsilon}_n)$ are the reflection and transmission coefficients, respectively, for a p-polarized wave incident upon the dioxide/substrate interface from the dioxide and having the in-plane wave vector component $k_x = \frac{n\omega}{c} \sin\theta$

The amplitudes $E^{\pm}_{n\omega,q}$ can be treated as the components of the two-component column vector $\mathbf{a}_{n\omega,q}$:

$$\mathbf{a}_{n\omega,q} = \begin{pmatrix} E^{+}_{n\omega,q} \\ E^{-}_{n\omega,q} \end{pmatrix}. \tag{10}$$

Under the assumption of factorability of the nonlocal conductivity tensor σ (which is justified for the nonlocal response of quantum wells), an effective transfer-matrix technique can be developed (see the Appendix), enabling one to relate the amplitude vectors $\mathbf{a}_{n\omega,q}$ and $\mathbf{a}_{n\omega,q+1}$ by means of the generalized transfer matrices [Eqs. (A24) and (A25) for $n=1$ and Eqs. (A35) and (A36) for $n=2$]. Thus the calculation of the local fields propagating at ω and 2ω in the MQW structure reduces to multiplying the corresponding matrices.

The SH intensity being measured in the experiment is determined by $E^{-}_{2\omega,0}$:

$$I_{2\omega} = \frac{c}{4\pi} |E^{-}_{2\omega,0}|^2. \tag{11}$$

The amplitude $E^{-}_{2\omega,0}$ is determined by Eqs. (A41)–(A44).

C. Model description of resonant properties

In order to specify the conductivity tensors σ and Σ we consider a simplified microscopic model, nonetheless retaining essential resonant features of the optical response of a single quantum well. Since the electron tunneling between neighboring quantum wells is strongly suppressed because of a large value of the band gap width in dioxide layers, it is sufficient to calculate σ and Σ for a single quantum well, with no regard for the presence of the other quantum wells and the substrate. For simplicity we neglect amorphousness and in-plane (azimuthal) anisotropy of the quantum well material, grounding our treatment on the concepts of quantum mechanics of the electron motion in crystalline solids.

Let us consider a quantum well occupying the region $0 \leqslant z \leqslant d$. The well boundaries are assumed to be infinite potential barriers, which necessitates the vanishing of the electron wave function at $z=0$ and $z=d$. We suppose that the electron motion in the xy plane is characterized by a parabolic isotropic dispersion relation, whereas the dispersion relation for the electron motion across the quantum well may differ from a parabolic one. Then a stationary electronic state has the wave function Φ,

$$\Phi^{(b)}_{j,\mathbf{p}}(\mathbf{r}, z) = \frac{1}{2\pi} \exp\frac{i\mathbf{p}\mathbf{r}}{\hbar} \varphi^{(b)}_j(z), \tag{12}$$

$$\varphi^{(b)}_j(z) = \sqrt{\frac{2}{d}} \sin\left(\frac{\pi j z}{d}\right),$$

$$j = 1,2, \ldots, \tag{13}$$

and the energy $\mathcal{E}$,

$$\mathcal{E}^{(b)}_j(\mathbf{p}) = \epsilon^{(b)}_j + \frac{\mathbf{p}^2}{2m^{(b)}_{\parallel}}, \tag{14}$$

$$\epsilon^{(b)}_j = \mathcal{E}^{(b)}_{\perp}(p_z)|_{p_z = \pi\hbar j/d}, \tag{15}$$

where $\mathbf{r}$ is the radius-vector parallel to the quantum well plane, $\mathbf{p}$ and p_z are the quasimomentum components parallel and normal to the quantum-well plane, respectively, $m^{(b)}_{\parallel}$ is the effective mass characterizing the in-plane electron motion, the function $\mathcal{E}^{(b)}_{\perp}(p_z)$ is the dispersion law for the electron motion in the z direction (in the bulk crystal), and $b = \mathrm{c}, \mathrm{v}$; the superscript c(v) denotes that a quantity pertains to an electronic state with the energy belonging to the conduction (valence) band of the spectrum of the bulk crystal.

To calculate the nonlocal conductivity tensors σ and Σ we use a resonant two-subband approximation by taking into account optical transitions between the electronic states from only two subbands, $\mathcal{E}^{(\mathrm{v})}_j(\mathbf{p})$ and $\mathcal{E}^{(\mathrm{c})}_{j'}(\mathbf{p})$, for which the resonance condition holds: $\Delta_{j'j} \equiv \epsilon^{(\mathrm{c})}_{j'} - \epsilon^{(\mathrm{v})}_j \approx n\omega$, where $n=1$ or $n=2$. In what follows we put, for simplicity, $m^{(\mathrm{c})}_{\parallel} = -m^{(\mathrm{v})}_{\parallel} = m$ (where m is the mass of an electron) and introduce an additional parameter Π by setting $|\mathbf{p}| \leqslant \Pi$, where $\Pi \lesssim \frac{\pi}{a}$ with a being the lattice constant. In other words, $|\mathbf{p}|$ is assumed to have the upper limit other than that corresponding to the boundary of the first Brillouin zone. Treating Π as an adjustable parameter allows us to regulate, in a simplest phenomenological manner, the magnitude of the resonant contribution to σ and Σ against the nonresonant background.

These assumptions lead to the following explicit expressions for the nonzero components of σ and Σ:

$$\sigma_{zz}(z,z',\omega) = -\frac{ie^2}{8\pi m\omega} S_{+}(\omega + i/\tau) \zeta_{j'j}(z) \zeta_{j'j}(z'), \tag{16}$$

$$\Sigma_{zxx}(z,z',z'',\omega) = \frac{ie^3}{16\pi m\hbar\omega^2} S_{-}(\omega + i/\tau) \zeta_{j'j}(z) \varphi^{(\mathrm{v})}_j(z') \times \varphi^{(\mathrm{c})}_{j'}(z') \delta(z' - z''), \tag{17}$$

$$\Sigma_{xxz}(z,z',z'',\omega) = -\frac{ie^3}{8\pi m\hbar\omega^2} S_{-}(\omega + i/\tau) \varphi^{(\mathrm{v})}_j(z) \times \varphi^{(\mathrm{c})}_{j'}(z) \delta(z - z') \zeta_{j'j}(z''), \tag{18}$$

$$\Sigma_{zzz} = \Sigma_{zxx} + \Sigma_{xxz}, \tag{19}$$

$$S_{\pm}(\Omega) = S(\Omega) \pm S(-\Omega), \quad S(\Omega) = \ln\left(\frac{\frac{\Pi^2}{m} + \Delta_{j'j} + \hbar\Omega}{\Delta_{j'j} + \hbar\Omega}\right), \tag{20}$$

$$\zeta_{j'j}(z) = \varphi_{j'}^{(c)}(z)\frac{d\varphi_j^{(v)}}{dz} - \varphi_j^{(v)}(z)\frac{d\varphi_{j'}^{(c)}}{dz}, \tag{21}$$

where τ is the relaxation time which is supposed, for simplicity, to have the same value for all electronic states in both valence and conduction bands.

It can be seen from Eqs. (16)–(19) that the peak position in the SHG spectrum is driven by $\Delta_{j'j}$. According to Eq. (15), the size dependence $\Delta_{j'j}(d)$ in turn is determined by the dispersion relations $\mathcal{E}_{\perp}^{(v)}(p_z)$ and $\mathcal{E}_{\perp}^{(c)}(p_z)$ for the energy of the electron motion in the z direction (in the bulk crystal). Assuming occurrence of the indirect band gap for the corresponding p_z direction in the quasimomentum space, we use the following phenomenological expressions:

$$\mathcal{E}_{\perp}^{(c)}(p_z) = \frac{\mathcal{E}_g}{2} + \mathcal{E}_c H\left(\frac{p_z - P}{\sqrt{m\mathcal{E}_c}}\right), \tag{22}$$

$$\mathcal{E}_{\perp}^{(v)}(p_z) = -\frac{\mathcal{E}_g}{2} - \mathcal{E}_v H\left(\frac{p_z}{\sqrt{m\mathcal{E}_v}}\right), \tag{23}$$

$$H(x) = 1 - \frac{1}{\cosh x}, \tag{24}$$

where $\mathcal{E}_g$, $\mathcal{E}_v$, and $\mathcal{E}_c$ are the widths of the (indirect) band gap, valence band, and conduction band along the p_z direction in the quasimomentum space, respectively; in this direction the top of the valence band and the bottom of the conduction band are attained at points $p_z=0$ and $p_z=P$, respectively.

IV. DATA ANALYSIS AND NUMERICAL RESULTS

A. Phenomenological analysis

1. Samples morphology

The thickness values for the silicon wells and silicon dioxide barriers are obtained from x-ray reflectometry using the Levenberg-Marquardt method of the reverse-problem solution.[21,22] Resulting fitting curves are shown in Fig. 1. The average period thickness is evaluated by fitting the specular curve around the first Bragg peak. The angular distance of 0.3° between Bragg peaks corresponds to the difference of 0.33 nm in the period thickness, which is close to the expected one-monolayer thickness of 0.25 nm provided that the covalent-bond length is taken as an elementary step in the Si well thickness. The average period thickness appears to be 2.36 and 2.03 nm for samples 1 and 2, respectively. Under assumption that the SiO_2 layer thickness in both samples has the same value of 1.08 nm, the silicon well thickness is found to be 1.28 and 0.95 nm for samples 1 and 2, respectively, which is slightly larger than that expected. The difference of these values from the technological ones can be caused by thickness variation of the Si and SiO_2 layers during the magnetron sputtering. The interface uncertainty associated with a transition layer between silicon and silicon dioxide[23] is estimated to be 0.40 and 0.20 nm for samples 1 and 2, respectively. These values are close to the error of thickness determination about 0.30 nm estimated from accuracy of the rf sputtering rate of silicon and fused quartz targets. The interface roughness decreases the Bragg maxima intensity on the reflectometry curves, which is approximately 50 times smaller than that in the case of flat boundaries. However, the value of interface uncertainty, which is significant in comparison with the MQW period, is about one-monolayer thickness in silicon and close to the thickness of the transition layer obtained at Si/SiO_2 interfaces by x-ray reflectometry.[24] This also restricts the reliability of the x-ray reflectometry data measured for samples 3 and 4.

2. SHG anisotropy

Since the MQW structures under study are made from amorphous materials, the observed type of rotational anisotropy can originate from the sputtering geometry. The latter possesses a single reflection plane parallel to the sputtering direction and perpendicular to the substrate. The symmetry shows a one- or twofold component in azimuthal dependence of SH intensity. This is argued by the same symmetry of the azimuthal SHG dependences reported previously for similar Si/SiO_2 MQW structures.[7,9] A small fourfold component is revealed in the azimuthal SHG dependence for sample 4 (d =0.25 nm), which is apparently a contribution from the Si(001) substrate whose response resonantly increases in the vicinity of 4.3 eV due to the E_2 critical point of the bulk silicon band structure. Thus the symmetry of the rotational SHG dependences for all samples differs from a distinct fourfold symmetry characterizing the response of the Si(001) substrate proper (bottom panel in Fig. 2). This indicates that the contribution of the substrate is negligible at least for the anisotropic part of the total SHG signal from the MQW structure.

The symmetry of the azimuthal patterns implies several constraints on the components of the third-rank tensor of the effective dipole quadratic susceptibility $\chi^{(2)}$ characterizing the quadratic optical response of the MQW structure. First, the components $\chi_{\alpha\beta\gamma}^{(2)}$ with either one or three indices y should vanish in the Cartesian frame with the z axis normal to the quantum wells and x axis parallel to the sputtering direction. Second, according to Eq. (1), the tensor components, which in the same frame determine the third azimuthal Fourier harmonic of the SH field, namely, $\chi_{xxx}^{(2)}$, $\chi_{xyy}^{(2)}$, and $\chi_{yxy}^{(2)}$, should be negligible in comparison with the components that govern the amplitude E_0, $\chi_{zzz}^{(2)}$, $\chi_{zxx}^{(2)}=\chi_{zyy}^{(2)}$, and $\chi_{xzx}^{(2)}=\chi_{yzy}^{(2)}$, and with those contributing exclusively to the term with E_1: $\chi_{xzz}^{(2)}$ and $\chi_{zxz}^{(2)}$.

The modification of the azimuthal SH intensity patterns with the two-photon energy, namely, alternating their symmetry between twofold and onefold types, can be described by Eq. (1) by varying the anisotropy phase $\tilde{\varphi}$ as an adjustable

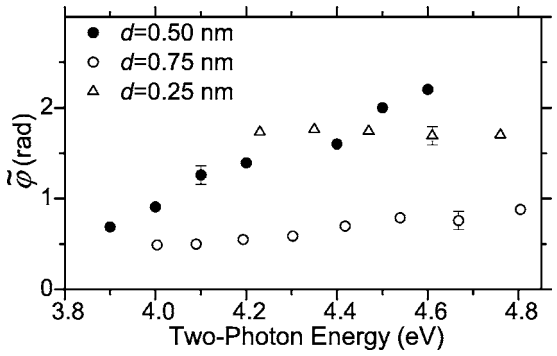

FIG. 6. Anisotropy phase $\tilde{\varphi}$ as a function of the two-photon energy for samples 2 (open circles), 3 (filled circles), and 4 (triangles). The values of $\tilde{\varphi}$ are obtained by fitting the expression given by Eq. (1) to the SH anisotropy data shown in Fig. 3.

parameter. For sample 3 the corresponding dependence of $\tilde{\varphi}$ on the two-photon energy is shown in Fig. 6 with filled circles. In the vicinity of 4.3 eV $\tilde{\varphi}$ is close to $\frac{\pi}{2}$, hence the components with amplitudes E_0 and E_1 contribute to the total SH field independently, which results in a twofold symmetry of the azimuthal SH intensity pattern. Below 4.0 eV and above 4.5 eV the E_0 and E_1 components interfere with each other, yielding a onefold symmetry of the azimuthal SHG dependence. For other MQW samples the spectral dependence of $\tilde{\varphi}$ is weak (Fig. 6): for a structure with thinner quantum wells $\tilde{\varphi}$ is close to $\frac{\pi}{2}$, whereas for that with thicker ones $\tilde{\varphi}$ tends to zero.

It is reasonable to interpret the spectral dependence of the anisotropy phase $\tilde{\varphi}$ as resulting from the different spatial localization of the nonlinear sources that generate the isotropic and anisotropic components of the SHG signal. The isotropic component with the amplitude E_0 is more likely associated with the sources distributed throughout all *a*-Si quantum wells, while the term with E_1 originates from the sources located in the quantum wells closest to the substrate. Under such assumption, the wavelength-dependent phase shift between the two components stems from retardation effects upon propagation of the SH field through the MQW structure.

3. SHG spectra

The shapes of MQW spectra (see Fig. 4) are different from that of the substrate spectrum, which has a peak at 3.3 eV attributed to the E_0'/E_1 critical point, and the peak at 4.3 eV attributed to the E_2 critical point of silicon. The shoulder at 3.8 eV is also seen in the substrate spectra. The observation and analysis of this shoulder has been reported by W. Daum and co-authors in Ref. 25 and attributed to transient silicon atoms between crystalline silicon and SiO_x. At 2.7 eV and 3.8–4 eV the SH intensity from the MQW samples is several times higher than the SHG signal from the bare substrate. Thus the conclusion drawn in the previous subsection on the substrate contribution to the total SHG signal can be strengthened in the following manner: both isotropic and anisotropic components of the substrate contribution to SHG are negligible in the spectral regions corresponding to resonances in the quadratic response of the MQW structure (simultaneously these regions turn out to be off-resonant for the quadratic response of the substrate). For this reason the quadratic response of the substrate will be ignored in calculations.

A narrow dip and sharp rise at the right edge of the idler range are present in the spectra of all samples and apparently reveal the influence of the substrate resonance. The dip can be caused by destructive interference between the contributions from the MQW and the substrate.[8] The same explanation is applicable to the dip at 4.25 eV observed in the spectrum of sample 4 (having the thinnest quantum wells).

The observed resonances in the vicinity of 2.7 eV are attributed to the direct inter-subband electron transitions in Si quantum wells, whose band structure (combined density of states specrum) is strongly modified by quantization effect. According to the results of linear-optical measurements,[2,17] the lowest resonances in the electron spectrum of Si-SiO_2 MQWs with the same parameters are located in the interval from 1.2 to 1.5 eV. Thus resonant features in the SHG spectra around 2.7 eV are reasonable to associate with one-photon resonance of quadratic susceptibility at the fundamental frequency. SHG resonances around 4.0 eV are new and were not studied by linear optics techniques. One of the possible explanations of their origin is the direct electron transitions in Si quantum wells between high-order subbands. In this case they can be associated with one-photon resonances of quadratic susceptibility at the fundamental frequency around 2 eV. However, the spectral position of these resonances close to the two-photon resonance of the Si substrate at 3.8 eV allows another description of features at 4.0 eV as resonant electron transitions attributed to transient silicon atoms at the interface between amorphous silicon and SiO_x, following Ref. 25.

The modification of the SH intensity spectra with the azimuthal angle depends on the quantum well thickness. For samples 1 and 2 (i.e., for those with thicker quantum wells) the spectrum shapes at ψ_0 and $\psi_\pm$ look similar. By contrast, for samples 3 and 4 (having thinner quantum wells) the spectrum shapes at ψ_0, ψ_-, and ψ_+ are quite different. Such behavior can be understood from the analysis of the azimuthal anisotropic dependences shown in Figs. 2 and 3: coherent superposition of the isotropic and anisotropic contributions to the quadratic response yields changes in the spectra shapes due to spectral dependence of the phase between these components, as shown in Fig. 6.

B. Numerical calculations

All numerical results presented in the following two subsections are obtained at $\varepsilon_1=\varepsilon_2=2.7$ and values of $\bar{\varepsilon}_{1,2}$ taken from Ref. 26. For the substrate the use of the bulk values of $\bar{\varepsilon}_{1,2}$ is justified by the substrate thickness, too large to expect the modification of $\bar{\varepsilon}$ by the size effect. For the dioxide layers the use of the bulk value seems reasonable since its nonresonant character within the spectral range of interest cannot be essentially affected by the finite layer thickness.

The resonance condition is assumed to be matched at the fundamental frequency.

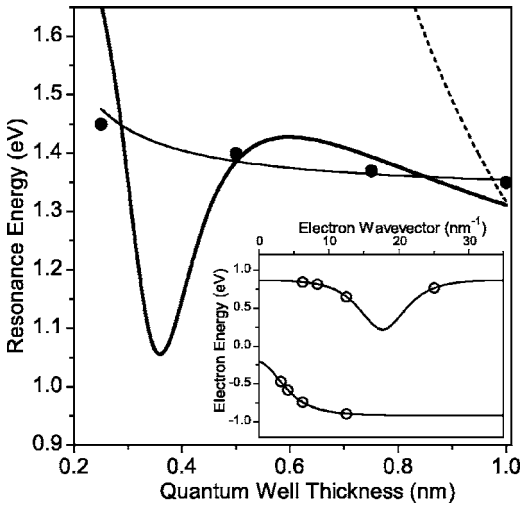

FIG. 7. Size effect in the position of the resonant peak of the the SH intensity spectrum. Thick solid line, fitting results at $\mathcal{E}_g = 0.43$ eV, $\mathcal{E}_v = 0.70$ eV, $\mathcal{E}_c = 0.65$ eV, and $P = 17.70$ nm^{-1}; the corresponding model dispersion law for the energy of the electron motion in the z direction is shown in inset. Shown for comparison: thin solid line, results of Ref. 8 for the model taking into account the interfacial distortions of the lattice potential; dashed line, the d^{-2} dependence for the infinite-barrier model. Solid circles, experimental values estimated from the SH intensity spectra shown in Fig. 4. Open circles in the inset correspond to the quantized values of the quasimomentum p_z at $j = 1$ (valence band), $j' = 2$ (conduction band), and the respective experimental values of the quantum-well thickness.

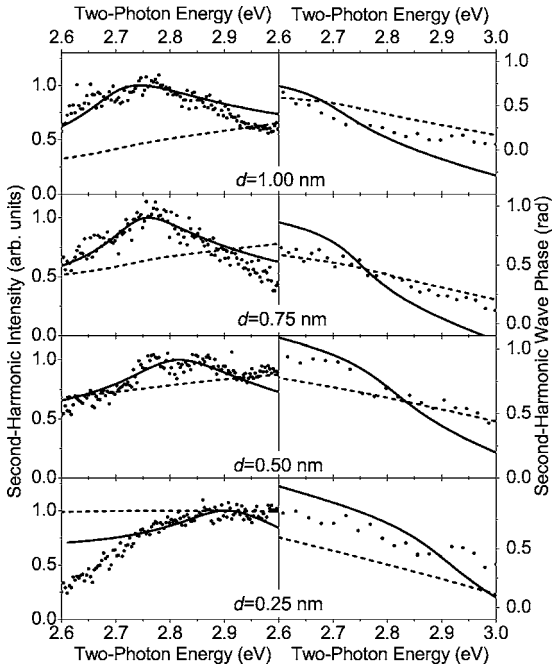

FIG. 8. Solid lines: the SH intensity (left panels) and relative wave phase (right panels) spectra calculated at $\Pi = 10.30$ nm^{-1} and $\hbar/\tau = 0.035$, 0.028, 0.040, and 0.040 eV for $d = 1.00$, 0.75, 0.50, and 0.25 nm, respectively. Filled circles: experimental data (same as in Figs. 4 and 5). Dashed lines: the modulus squared (left panels) and phase (right panels) of the corresponding structural factor Q, expressed in the same arbitrary units as the SH intensity, and in radians, respectively.

1. Size effect in the peak position

In the present model the size effect in the peak position in the SH intensity spectrum is determined by the function $\Delta_{jj'}(d) = \epsilon_{j'}^{(c)}(d) - \epsilon_j^{(v)}(d)$ with $\epsilon_j^{(v)}(d)$ and $\epsilon_{j'}^{(c)}(d)$ given by Eqs. (15) and (22)–(24). The occurrence of the indirect band gap leads to a nonmonotonous thickness dependence $\Delta_{jj'}(d)$ (thick solid curve in Fig. 7), in contrast to the monotonous one resulting from the distortions of the lattice potential at the interfaces of the MQW structure[8] (thin solid curve in Fig. 8). However, for the discrete set of the values of d corresponding to the quantum well thicknesses in the studied samples, the dependence $\Delta_{jj'}(d)$ reproduces the observed size effect in the peak position much better than the d^{-2} dependence (dashed line in Fig. 7) obtained within the framework of the infinite-barrier model with a direct band gap and parabolic dispersion law in both valence and conduction bands.

2. SH intensity and phase spectra

Figure 8 shows the SH intensity and relative phase spectra obtained by fitting the dependences derived in Sec. III to the experimental data. Within the resonant two-subband approximation used in the model only a single-peak intensity spectrum can be reproduced. For that reason the calculations are carried out for the limited interval of 2.6–3.0 eV containing the main peaks of all SH intensity spectra measured in the idler range.

The influence of the wave propagation through the multilayer nonlocal medium on the outgoing SH signal can be characterized by the complex structural factor $Q = |Q|e^{i\phi_Q}$, which we define as the coefficient relating the amplitude $E_{2\omega,0}^-$ given by Eq. (A41) with the function S that determines the resonant properties of an individual quantum well as given by Eqs. (16)–(21):

$$E_{2\omega,0}^- = QS(\omega + i/\tau). \tag{25}$$

The spectra of $|Q|^2$ and ϕ_Q extracted from the calculated spectra of the SH intensity and relative wave phase are shown in Fig. 8 with dashed lines.

According to Fig. 9, the peak width characterizing the SH intensity spectrum is sensitive to the total number of quantum wells N to a much greater extent than the peak position. Noteworthily, both peak width and position depend on N nonmonotonously.

V. CONCLUSIONS

To summarize, Si/SiO_2 multiple quantum wells with subnanometer values of the silicon quantum well thickness have been studied experimentally and theoretically. The x-ray diffraction measurements confirmed that in the subnanometer thickness range the samples retain uniformly periodic structure. The nonlinear optical studies combining spectroscopy and interferometric spectroscopy of second-harmonic gen-

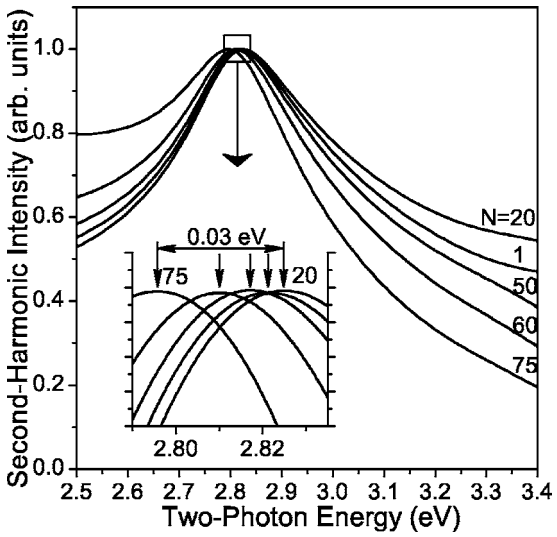

FIG. 9. SH intensity spectra calculated for the model MQW structure at $\Pi=10.30\ \mathrm{nm}^{-1}$, $\hbar\Delta_{12}=1.4$ eV, $\hbar/\tau=0.035$ eV, and $d=0.5$ nm for various numbers of quantum wells.

eration allowed measuring an extended set of parameters, including the relative second-harmonic wave phase and rotational anisotropy phase. The measured spectra revealed pronounced dependence on the quantum well thickness. In the theoretical aspect, the macroscopic approach to the description of the quadratic optical response of multiple quantum wells as piecewise-continuous nonlocal media has proven to be applicable to the interpretation of observed size effects on the subnanometer thickness scale.

ACKNOWLEDGMENTS

The authors wish to thank P.V. Elyutin for helpful discussions. This work was supported by the Russian Foundation for Basic Research, grants for Leading Russian Science Schools, and INTAS Grant No. 03-51-3784.

APPENDIX: GENERALIZED OPTICAL TRANSFER-MATRIX TECHNIQUE

The optical transfer-matrix technique[19] applicable to SHG in a layered medium with local linear and quadratic response can be generalized to the case of an MQW structure considered in Sec. III, with both linear and quadratic response of quantum wells being essentially nonlocal in the direction normal to their boundaries.

1. Local response

Consider two local homogeneous media I and II having dielectric constants ε^I and ε^{II}, respectively, and separated at point $z=Z$ by a flat interface. Then the relation between the corresponding amplitudes $\mathbf{a}_I$ and $\mathbf{a}_{II}$ reads[19]

$$\mathbf{a}_I = \mathsf{M}(Z,\varepsilon^I,\varepsilon^{II})\cdot\mathbf{a}_{II}, \tag{A1}$$

$$\mathsf{M}(Z,\varepsilon^I,\varepsilon^{II}) = \mathsf{U}(-\kappa^I Z)\cdot\mathsf{M}(\varepsilon^I,\varepsilon^{II})\cdot\mathsf{U}(\kappa^{II}Z), \tag{A2}$$

with the propagation matrix

$$\mathsf{U}(\xi) = \begin{pmatrix} e^{i\xi} & 0 \\ 0 & e^{-i\xi} \end{pmatrix} \tag{A3}$$

and the transfer matrix

$$\mathsf{M}(\varepsilon^I,\varepsilon^{II}) = \frac{1}{t_\theta(\varepsilon^I,\varepsilon^{II})}\begin{pmatrix} 1 & r_\theta(\varepsilon^I,\varepsilon^{II}) \\ r_\theta(\varepsilon^I,\varepsilon^{II}) & 1 \end{pmatrix}, \tag{A4}$$

where $\kappa^{I,II}=\frac{\omega}{c}\sqrt{\varepsilon^{I,II}-\sin^2\theta}$, and $r_\theta(\varepsilon^I,\varepsilon^{II})$ and $t_\theta(\varepsilon^I,\varepsilon^{II})$ are the reflection and transmission coefficients, respectively, for a p-polarized wave incident upon the interface from the medium I and having the in-plane wave vector component $k_x=\frac{\omega}{c}\sin\theta$.

2. Nonlocal response at ω

The local field in the MQW structure satisfies the self-consistent integral equation:[14]

$$\mathbf{E}_\omega(z) = \mathbf{E}_{\mathrm{h}1}(z) + \gamma\sum_q \hat{G}_\omega^{(q)}\cdot\hat{\sigma}_\omega^{(q)}\cdot\mathbf{E}_\omega^{(q)}(z), \tag{A5}$$

with

$$\hat{G}_\omega^{(q)}\cdot\mathbf{f}(z) = \int_{ql-d}^{ql} G_{\omega,\theta}(z,z')\cdot\mathbf{f}(z')dz', \tag{A6}$$

where $\gamma=-4\pi i\omega/c^2$, $\mathbf{E}_\omega^{(q)}(z)$ is the local field inside the qth quantum well, $\mathbf{E}_{\mathrm{h}1}(z)$ is the local field in the host medium, and $G_{\omega,\theta}(z,z')$ is the tensorial Green's function of the electromagnetic field with frequency ω and in-plane wave vector component $k_x=\frac{\omega}{c}\sin\theta$ in the host medium. The latter is obtained from the MQW structure removing the quantum wells so that the corresponding regions become vacuum layers with the unit dielectric constant.

Let the coordinates z and z' satisfy the conditions

$$(q-1)l \leqslant z \leqslant ql + D, \tag{A7}$$

$$ql - d \leqslant z' \leqslant ql, \tag{A8}$$

i.e., z lies within the qth quantum well with the adjacent qth and $(q+1)$th dioxide layers, whereas z' is located within the qth quantum well. In order to deal with a structurally less-complicated system, for z and z' lying within the specified regions we represent $G_\omega(z,z')$ as

$$G_{\omega,\theta}(z,z') = g_{\omega,\theta}^{(q)}(z,z') + \mathcal{G}_{\omega,\theta}^{(q)}(z,z'), \tag{A9}$$

$$\mathcal{G}_{\omega,\theta}^{(q)}(z,z') = \mathcal{G}_{\omega,\theta}(z-z_q,z'-z_q), \tag{A10}$$

where $z_q=ql-\frac{d}{2}$ and $\mathcal{G}_{\omega,\theta}(z,z')$ is the tensorial Green's function of the electromagnetic field with frequency ω and in-plane wave vector component $\frac{\omega}{c}\sin\theta$ in a three-layer host medium: the layer $-\frac{d}{2}\leqslant z\leqslant\frac{d}{2}$ corresponds to vacuum, whereas the half-spaces $z<-\frac{d}{2}$ and $z>\frac{d}{2}$ are occupied by the dioxide. The explicit expressions for the components of $\mathcal{G}_{\omega,\theta}$ are omitted for brevity. Introducing by analogy with Eq. (A6) the integral operators $\hat{g}_\omega^{(q)}$ and $\mathcal{G}_\omega^{(q)}$, we rewrite Eq. (A5) as follows:

$$\mathbf{E}_{\omega}^{(q)}(z) = \tilde{\mathbf{E}}_{\omega}^{(q)}(z) + \gamma\hat{\mathcal{G}}_{\omega}^{(q)} \cdot \hat{\sigma}_{\omega}^{(q)} \cdot \mathbf{E}_{\omega}^{(q)}(z), \tag{A11}$$

where the field

$$\tilde{\mathbf{E}}_{\omega}^{(q)}(z) = \mathbf{E}_{\mathrm{h}}^{(q)}(z) + \gamma\left(\hat{g}_{\omega}^{(q)} \cdot \mathbf{j}_{\omega}^{(q)}(z) + \sum_{q' \neq q} \hat{G}_{\omega}^{(q')} \cdot \mathbf{j}_{\omega}^{(q')}(z)\right) \tag{A12}$$

will be referred to as the background one.

Further procedure is based on three essential points.

(*i*) That part of the tensor $\mathcal{G}_{\omega,\theta}(z,z')$ which contributes to *p*-polarized radiation has, within the regions of interest, the following dyadic form:

$$\mathcal{G}_{\omega,\theta}^{\mathrm{p\text{-}p}}\left(z < -\frac{d}{2}, -\frac{d}{2} \leqslant z' \leqslant \frac{d}{2}\right) = e^{-i\kappa_1 z}\mathbf{e}_{-}\mathbf{G}_{\omega}(z'), \tag{A13}$$

$$\mathcal{G}_{\omega,\theta}^{\mathrm{p\text{-}p}}\left(z > \frac{d}{2}, -\frac{d}{2} \leqslant z' \leqslant \frac{d}{2}\right) = e^{i\kappa_1 z}\mathbf{e}_{+}\mathbf{G}_{\omega}(-z'), \tag{A14}$$

where $\mathbf{G}_{\omega}(z)$ is a known vector function ($G_{\omega,y} \equiv 0$).

(*ii*) The background field has the form analogous to that given by Eq. (5), i.e., it is a superposition of a rightward- and leftward-propagating waves. Inside the *q*th quantum well

$$\tilde{\mathbf{E}}_{\omega}^{(q)}(z) = \tilde{E}_{\omega}^{(q)+}\mathbf{e}_{+}e^{ik_z z} + \tilde{E}_{\omega}^{(q)-}\mathbf{e}_{-}e^{-ik_z z}. \tag{A15}$$

The corresponding two-component amplitude vector is

$$\tilde{\mathbf{a}}_{\omega}^{(q)} = \begin{pmatrix} \tilde{E}_{\omega}^{(q)+} \\ \tilde{E}_{\omega}^{(q)-} \end{pmatrix}. \tag{A16}$$

Inside the *q*th and $(q+1)$th dioxide layers the background field amplitudes, $\tilde{\mathbf{a}}_{\omega,q}$ and $\tilde{\mathbf{a}}_{\omega,q+1}$, can be related to $\tilde{\mathbf{a}}_{\omega}^{(q)}$ with the use of the matrices given by Eqs. (A2)–(A4):

$$\tilde{\mathbf{a}}_{\omega,q} = \mathsf{M}(ql - d, \varepsilon_1, 1) \cdot \tilde{\mathbf{a}}_{\omega}^{(q)}. \tag{A17}$$

$$\tilde{\mathbf{a}}_{\omega,q+1} = \mathsf{M}(ql, \varepsilon_1, 1) \cdot \tilde{\mathbf{a}}_{\omega}^{(q)}. \tag{A18}$$

(*iii*) Upon treating the background field $\tilde{\mathbf{E}}_{\omega}^{(q)}(z)$ as given, Eq. (A11) can be solved explicitly under assumption that the linear conductivity tensor $\sigma(z,z',\omega)$ is factorable, which is justified for description of the resonant optical response of a quantum well:

$$\sigma(z,z',\omega) = \zeta(z)\zeta(z')\sigma(\omega), \tag{A19}$$

where $\zeta(z)$ and $\sigma(\omega)$ are known scalar function and second-rank tensor, respectively. Under this condition the problem reduces to an algebraic one that yields the following explicit solution of Eq. (A11):

$$\mathbf{E}_{\omega}^{(q)}(z) = \tilde{\mathbf{E}}_{\omega}^{(q)}(z) + \gamma\mathcal{G}_{\omega}^{(q)}(z) \cdot (I - \gamma\mathcal{G}_{\omega})^{-1} \cdot \tilde{\mathbf{E}}_{\omega}^{(q)}, \tag{A20}$$

where I is the unit tensor and

$$\tilde{\mathbf{E}}_{\omega}^{(q)} = \int_0^d \tilde{\mathbf{E}}_{\omega}^{(q)}(z' + ql - d)\zeta(z')dz', \tag{A21}$$

$$\mathcal{G}_{\omega}^{(q)}(z) = \int_{-d/2}^{d/2} \mathcal{G}_{\omega,\theta}^{(q)}(z,z')\zeta(z')dz' \cdot \sigma_1, \tag{A22}$$

$$\mathcal{G}_{\omega} = \int_{-d/2}^{d/2}\int_{-d/2}^{d/2} \mathcal{G}_{\omega,\theta}(z',z'')\zeta(z')\zeta(z'')dz'dz'' \cdot \sigma_1 \tag{A23}$$

with $\sigma_1 = \sigma(\omega)$.

On these grounds, from Eqs. (A13), (A14), (A17), (A18), and (A20)–(A23) we obtain the sought generalization of Eq. (A1) to the case of dielectric layers separated by slabs with a factorable nonlocal linear conductivity tensor. Namely, the relation between the amplitude vectors $\mathbf{a}_{\omega,q}$ and $\mathbf{a}_{\omega,q+1}$ of the local electric field inside the *q*th and $(q+1)$th dioxide layers reads

$$\mathbf{a}_{\omega,q} = \underline{\mathsf{M}}_{\omega}(z_q) \cdot \mathbf{a}_{\omega,q+1}, \tag{A24}$$

$$\underline{\mathsf{M}}_{\omega}(z) = \mathsf{U}(-\kappa_1 z) \cdot \underline{\mathsf{M}}_{\omega} \cdot \mathsf{U}(\kappa_1 z), \tag{A25}$$

with the generalized transfer matrix

$$\underline{\mathsf{M}}_{n\omega} = \left[\mathsf{M}\left(-\frac{nd}{2}, \varepsilon_n, 1\right) + \mathsf{C}_{n\omega}^{-}\right] \cdot \left[\mathsf{M}\left(\frac{nd}{2}, \varepsilon_n, 1\right) + \mathsf{C}_{n\omega}^{+}\right]^{-1}, \tag{A26}$$

where

$$\mathsf{C}_{n\omega}^{+} = \begin{pmatrix} C_{n\omega}^{++} & C_{n\omega}^{+-} \\ 0 & 0 \end{pmatrix}, \quad \mathsf{C}_{n\omega}^{-} = \begin{pmatrix} 0 & 0 \\ C_{n\omega}^{-+} & C_{n\omega}^{--} \end{pmatrix},$$

$$C_{n\omega}^{\mu\nu} = n\gamma s_{n\omega}^{\mu\nu},$$

$$s_{n\omega}^{\mu\nu} = \mathbf{e}_{\mu} \cdot \mathbf{G}_{n\omega}^{\mu} \cdot \sigma_n \cdot (\zeta_n^{\nu} I + \Gamma_{n\omega}) \cdot \mathbf{e}_{\nu},$$

$$\Gamma_{n\omega} = \mathcal{G}_{n\omega} \cdot (I - n\gamma\sigma_n \cdot \mathcal{G}_{n\omega})^{-1}$$

$$\mathbf{G}_{n\omega}^{\mu} = \int_{-d/2}^{d/2} \mathbf{G}_{n\omega}(\varsigma_{\mu} z)\zeta(z)dz,$$

$$\zeta_n^{\nu} = \int_{-d/2}^{d/2} \zeta(z)e^{in\varsigma_{\nu}k_z z}dz, \quad \varsigma_{\pm} = \pm 1,$$

$$\mu, \nu = +, - . \quad n = 1,2.$$

From Eqs. (A24)–(A26) and conditions (6)–(8) at the outermost interfaces at frequency ω, we obtain an expression for the amplitude vector $\mathbf{a}_{\omega,q}$ in the *q*th dioxide layer:

$$\mathbf{a}_{\omega,q\geqslant 1} = \mathsf{A}_{\omega}(q-1) \cdot \mathsf{M}(\varepsilon_1, 1) \cdot \mathbf{a}_{\omega,0}, \tag{A27}$$

$$\mathsf{A}_{n\omega}(q) = \mathsf{U}(-\kappa_n z_q) \cdot [\underline{\mathsf{M}}_{n\omega}^{-1} \cdot \mathsf{U}(\kappa_n l)]^q \cdot \mathsf{U}(-\kappa_n d/2),$$

$$n = 1,2, \tag{A28}$$

where

$$\mathbf{a}_{\omega,0} = E_{\mathrm{f}}\begin{pmatrix} 1 \\ b_1^{-}/b_1^{+} \end{pmatrix},$$

$$\begin{pmatrix} b_1^+ \\ b_1^- \end{pmatrix} = \mathsf{M}(1,\varepsilon_1) \cdot \mathsf{A}_\omega^{-1}(N) \cdot \begin{pmatrix} 1 \\ r(\varepsilon_1,\bar{\varepsilon}_1)e^{2i\kappa_1 L} \end{pmatrix},$$

Once $\mathbf{a}_{\omega,q}$ is found, an explicit expression for the local field amplitude $\mathbf{a}_\omega^{(q)}$ inside the qth quantum well can be derived from Eqs. (A17) and (A20).

3. Nonlocal response at 2ω

At frequency 2ω the local field satisfies the self-consistent integral equation:

$$\mathbf{E}_{2\omega}(z) = \mathbf{E}_{\mathrm{h}2}(z) + 2\gamma \sum_q \hat{G}_{2\omega}^{(q)} \cdot \hat{\sigma}_{2\omega}^{(q)} \cdot \mathbf{E}_{2\omega}^{(q)}(z), \quad \text{(A29)}$$

where $\mathbf{E}_{\mathrm{h}2}(z)$ is the local field produced in the MQW host medium by the nonlinear currents $\mathbf{J}^{(q)}(z)$ and $\bar{\mathbf{J}}$:

$$\mathbf{E}_{\mathrm{h}2}(z) = \bar{\mathbf{E}}_{\mathrm{h}2}(z) + \sum_q \mathbf{E}_{\mathrm{h}2}(z;q), \quad \text{(A30)}$$

$$\bar{\mathbf{E}}_{\mathrm{h}2}(z) = 2\gamma G_{2\omega,\theta}(z, L+0) \cdot \bar{\mathbf{J}}(z), \quad \text{(A31)}$$

$$\mathbf{E}_{\mathrm{h}2}(z;q) = 2\gamma \hat{G}_{2\omega}^{(q)} \cdot \mathbf{J}^{(q)}(z). \quad \text{(A32)}$$

From Eq. (A29) we obtain an analog of Eq. (A11) for the field $\mathbf{E}_{2\omega}^{(q)}(z)$ inside the qth quantum well:

$$\mathbf{E}_{2\omega}^{(q)}(z) = \tilde{\mathbf{E}}_{2\omega}^{(q)}(z) + \mathbf{E}_{\mathrm{h}2}^{(q)}(z;q) + 2\gamma \hat{\mathcal{G}}_{2\omega}^{(q)} \cdot \hat{\sigma}_\omega^{(q)} \cdot \mathbf{E}_{2\omega}^{(q)}(z), \quad \text{(A33)}$$

where the background field $\tilde{\mathbf{E}}_{2\omega}^{(q)}(z)$ takes the form

$$\tilde{\mathbf{E}}_{2\omega}^{(q)}(z) = \bar{\mathbf{E}}_{\mathrm{h}2}^{(q)}(z) + \sum_{q' \neq q} \mathbf{E}_{\mathrm{h}2}^{(q)}(z;q') + 2\gamma \left(\hat{g}_{2\omega}^{(q)} \cdot \mathbf{j}_{2\omega}^{(q)}(z) + \sum_{q' \neq q} \hat{G}_{2\omega}^{(q')} \cdot \mathbf{j}_{2\omega}^{(q')}(z) \right). \quad \text{(A34)}$$

Under the assumption of factorability of the linear conductivity [as given by Eq. (A19)], the solution of Eq. (A33) yields an analog of Eq. (A24) for the amplitude vectors $\mathbf{a}_{2\omega,q}$ and $\mathbf{a}_{2\omega,q+1}$ inside the qth and $(q+1)$th dioxide layers:

$$\mathbf{a}_{2\omega,q} = \underline{\mathsf{M}}_{2\omega}(z_q) \cdot \mathbf{a}_{2\omega,q+1} + \mathbf{v}^{(q)}, \quad \text{(A35)}$$

$$\mathbf{v}^{(q)} = \begin{pmatrix} 0 \\ v_-^{(q)} \end{pmatrix} + \underline{\mathsf{M}}_{2\omega}(z_q) \cdot \begin{pmatrix} v_+^{(q)} \\ 0 \end{pmatrix}, \quad \text{(A36)}$$

where the term $\mathbf{v}^{(q)}$ [appearing in Eq. (A35) due to the presence of the nonlinear current $\mathbf{J}^{(q)}$ inside the qth quantum well] has the components

$$v_\pm^{(q)} = 2\gamma e^{\mp i\kappa_{2z} z_q} \int_{-d/2}^{d/2} \mathbf{G}_{2\omega}(\mp z') \cdot \mathbf{J}^{(q)}(z' + z_q) dz'. \quad \text{(A37)}$$

From Eq. (A35) and conditions (7) and (8) at the outermost interfaces at frequency 2ω we finally find

$$\mathbf{a}_{2\omega,q\geq 1} = \mathsf{A}_{2\omega}(q-1) \cdot \mathsf{M}(\varepsilon_2,1) \cdot \mathbf{a}_{2\omega,0} + \mathbf{w}^{(q-1)}, \quad \text{(A38)}$$

$$\mathbf{w}^{(0)} = 0, \quad \mathbf{w}^{(q\geq 1)} = -\sum_{q'=1}^{q} \mathsf{A}_{2\omega}(q-q') \cdot \mathbf{v}^{(q')}, \quad \text{(A39)}$$

where

$$\mathbf{a}_{2\omega,0} = \begin{pmatrix} 0 \\ E_{2\omega,0}^- \end{pmatrix}, \quad \text{(A40)}$$

$$E_{2\omega,0}^- = u_- - \frac{b_2^-}{b_2^+} u_+, \quad \text{(A41)}$$

$$\begin{pmatrix} b_2^+ \\ b_2^- \end{pmatrix} = \mathsf{M}(1,\varepsilon_2) \cdot \mathsf{A}_{2\omega}^{-1}(N) \cdot \begin{pmatrix} 1 \\ r(\varepsilon_2,\bar{\varepsilon}_2)e^{2i\kappa_2 L} \end{pmatrix}, \quad \text{(A42)}$$

$$\begin{pmatrix} u^+ \\ u^- \end{pmatrix} = \mathsf{M}(1,\varepsilon_2) \cdot \mathbf{s}, \quad \text{(A43)}$$

$$\mathbf{s} = \mathbf{v}^{(1)} + \sum_{q'=2}^{N} \mathsf{A}_{2\omega}^{-1}(q'-1) \cdot \mathbf{v}^{(q')}. \quad \text{(A44)}$$

[1] A. F. Plotnikov, F. A. Pudonin, and V. B. Stopachinski, JETP Lett. **46**, 560 (1987).
[2] O. Keller, A. Liu, and A. Zayats, Opt. Commun. **110**, 604 (1994).
[3] D. J. Lockwood, Z. H. Lu, and J. M. Baribeau, Phys. Rev. Lett. **76**, 539 (1996).
[4] B. Averboukh, R. Huber, K. W. Cheah, Y. R. Shen, G. G. Qin, Z. C. Ma, and W. H. Zong, J. Appl. Phys. **92**, 3564 (2002).
[5] R. Sammynaiken, S. J. Naftel, T. K. Shamb, K. W. Cheah, B. Averboukh, R. Huber, Y. R. Shen, G. G. Qin, Z. C. Ma, and W. H. Zong, J. Appl. Phys. **92**, 3000 (2002).
[6] O. A. Aktsipetrov, V. N. Golovkina, A. I. Zayats, T. V. Murzina, A. A. Nikulin, and A. A. Fedyanin, Phys. Dokl. **40**, 171 (1995).
[7] O. A. Aktsipetrov, A. N. Rubtsov, A. V. Zayats, W. de Jong, C. W. van Hasselt, M. A. C. Devillers, T. Rasing, and E. D. Mishina, JETP **82**, 668 (1996).
[8] T. V. Dolgova, V. G. Avramenko, A. A. Nikulin, G. Marowsky, A. F. Pudonin, A. A. Fedyanin, and O. A. Aktsipetrov, Appl. Phys. B: Lasers Opt. **74**, 671 (2002).
[9] O. A. Aktsipetrov, P. V. Elyutin, A. A. Fedyanin, A. A. Nikulin, and A. N. Rubtsov, Surf. Sci. **325**, 343 (1995).
[10] O. A. Aktsipetrov and A. A. Fedyanin, Thin Solid Films **294**, 235 (1997).
[11] V. V. Savkin, A. A. Fedyanin, F. A. Pudonin, A. N. Rubtsov, and O. A. Aktsipetrov, Thin Solid Films **336**, 350 (1998).
[12] V. I. Gavrilenko, R. Q. Wu, M. C. Downer, J. G. Ekerdt, D. Lim, and P. Parkinson, Phys. Rev. B **63**, 165325 (2001).

[13] O. A. Aktsipetrov, P. V. Elyutin, E. V. Malinnikova, E. D. Mishina, A. N. Rubtsov, W. de Jong, and T. Raising, Phys. Dokl. **42**, 340 (1997).
[14] O. Keller, J. Opt. Soc. Am. B **12**, 987 (1995).
[15] O. Keller, J. Opt. Soc. Am. B **12**, 997 (1995).
[16] E. A. Vinogradov and G. I. Makarov, Sov. Phys. Solid State **31**, 1714 (1989).
[17] E. A. Vinogradov, A. V. Zayats, and F. A. Pudonin, Sov. Phys. Solid State **33**, 113 (1991).
[18] G. Lüpke, Surf. Sci. Rep. **35**, 75 (1999).
[19] D. S. Bethune, J. Opt. Soc. Am. B **6**, 910 (1989).
[20] T. V. Dolgova, A. A. Fedyanin, O. A. Aktsipetrov, and G. Marowsky, Phys. Rev. B **66**, 033305 (2002).
[21] M. K. Sanyal, S. Hazra, J. K. Basu, and A. Datta, Phys. Rev. B **58**, R4258 (1998).
[22] V. A. Bushuev, A. A. Lomov, and A. G. Sutyrin, Crystallogr. Rep. **47**, 683 (2002).
[23] R. A. Cowley and T. W. Ryan, J. Phys. D **20**, 61 (1987).
[24] J. A. Dura, C. A. Richter, C. F. Majkrzak, and N. V. Nguen, Appl. Phys. Lett. **73**, 2131 (1998).
[25] G. Erley and W. Daum, Phys. Rev. B **58**, R1734 (1998).
[26] D. E. Aspnes and A. A. Studna, Phys. Rev. B **27**, 985 (1983).